Assessment of nonalcoholic fatty liver function by photoacoustic imaging

Jinge Yang,[a,†] Tingting Qiu,[b,†] Teng Pan,[c,d] Guang Zhang,[c,d] Wenwu Ling,[b] Yuqing Zhou,[b] Yan Luo,[b] and Huabei Jiang[e,*]

[a]Chongqing University of Posts and Telecommunications, School of Optoelectric Engineering, Chongqing, China

[b]Sichuan University West China Hospital, Department of Medical Ultrasound, Chengdu, China

[c]University of Electronic Science and Technology of China, School of Electronic Science and Engineering (National Exemplary School of Microelectronics), Chengdu, China

[d]University of Electronic and Technology of China, Center for Information in Medicine, Chengdu, China

[e]University of South Florida, Department of Medical Engineering, Tampa, Florida, United States

Abstract

Significance: The assessment of liver function plays an important role in the diagnosis of nonalcoholic fatty liver disease (NAFLD). Current noninvasive imaging methods have limited applicability in this regard.

Aim: We report an application of multispectral photoacoustic imaging (PAI), an emerging modality, to visualize lipid accumulation and liver function in NAFLD.

Approach: We first demonstrated the liver function reserve with indocyanine green (ICG) to verify the organ's dysfunction due to NAFLD in a rabbit model. We then noninvasively quantified lipid content in the liver using multispectral PAI. The *in vivo* PAI results were compared and verified with photoacoustic *ex vivo* images and liver biopsy.

Results: A significant difference in the $\text{lipid}_{\text{mean}}$ value was observed [$\text{lipid}_{\text{mean}} = 0.081 \pm 0.0161$ arbitrary units (a.u.) control versus NAFLD 0.198 ± 0.048 a.u., $P = 0.003$]. Similar to *in vivo* analysis, a significant difference in $\text{lipid}_{\text{mean}}$ was observed ($\text{lipid}_{\text{mean}} = 0.0673 \pm 0.0165$ versus 0.486 ± 0.073 a.u., $P < 0.0001$) between control and NAFLD group *ex vivo*. For liver function, the control group showed a rapid decrease after the peak point, whereas the elimination of ICG for the NAFLD group was slower.

Conclusions: Our study shows that PAI has the potential to provide a noninvasive biomarker for the assessment of liver function and lipid accumulation for NAFLD diagnosis and treatment.

 [DOI: 10.1117/1.JBO.28.1.016003]

Keywords: indocyanine green; nonalcoholic fatty liver disease; photoacoustic imaging; liver function; lipid accumulation.

Paper 220175GRR received Jul. 30, 2022; accepted for publication Jan. 5, 2023; published online Jan. 25, 2023.

1 Introduction

Nonalcoholic fatty liver disease (NAFLD) is characterized by excessive hepatic fat accumulation associated with an increasing rate of obesity, diabetes, and metabolic syndrome. The prevalence of NAFLD is ~25% globally, afflicting about 1 billion individuals worldwide, which is

*Address all correspondence to Huabei Jiang, hjiang1@usf.edu

†These authors contributed equally to this work.

becoming the predominant cause of chronic liver disease and a substantial clinical and economic burden around the world.[1–3]

In the context of NAFLD, the first diagnostic requirement is to show the presence of fat in the liver accurately. The presence of fat >5% to 10% is considered abnormal.[1,4] Liver biopsy is the gold standard for the diagnosis and classification of NAFLD. However, it suffers from being invasive, expensive, associated with potential complications and sampling error, and plagued with interobserver variability.[5–7] Magnetic resonance spectroscopy or magnetic resonance imaging (MRI) quantifies the proton density fat fraction (PDFF) to measure hepatic triglyceride amount. However, both techniques are costly with restricted accessibility and high requirements for expertise.[2,8–10] Compared to MRI-PDFF, the transient elastography-based controlled attenuation parameter is less accurate for the diagnosis of hepatic steatosis.[11] Optical method, such as near-infrared hyperspectral imaging, can be an alternative that is a noninvasive, noncontact, nonionizing, and label-free technique. However, it suffers from penetration depth limitation due to the scattering of light.[12] Although a variety of techniques are available for hepatic steatosis evaluation, little is known about the liver function reserve (LFR) with the progression of NAFLD.[13] LFR is the remnant functional capacity of the liver after liver injury, which is considered an important factor for treatment and prognosis in chronic liver diseases. Indocyanine green (ICG) clearance test is the acknowledged approach for LFR assessment, the nature of which is to accurately detect ICG concentration change over time in blood. ICG can be selectively up taken by liver cells, eliminated to bile and excreted with feces through the bowel in the original form. ICG was not uptake by other organs or tissue and is an ideal drug for LFR reflection. In hepatic surgery, ICG retention rate at 15 min (ICGR15) < 30% is an essential condition for safe hepatectomy. ICGR15 > 40% is the contraindication for hepatectomy because posthepatectomy liver failure can occur with a large probability.[14–16]

Photoacoustic imaging (PAI) is an emerging noninvasive modality focusing on the measurement of optical absorption of endogenous or exogenous absorbers, which can afford high-resolution images in superficial or deep tissue. Its clinical applicability has been demonstrated in breast cancer, thyroid cancer, melanoma, arthritis, bowel disease,[17–21] and in the detection of endogenous molecular chromophores, such as melanin, hemoglobin, lipids, and collagen.[22–25] Steatosis in fatty liver mice diagnosed with PAI indicated a prominent difference from normal mice.[26–28] However, previous applications were focused on small animals. Here we want to test the feasibility in a larger animal model with similar imaging depth to check its potential for clinical translations. In addition, combining the LFR assessment by PAI with general contrast agents[29] and the multispectral method has not been demonstrated on large animal models. Based on this prior study,[29] the goal of the current study is to show that PAI is capable of not only assessing LFR but also visualizing lipid content in fatty liver rabbits and to demonstrate PAI as a new noninvasive imaging biomarker for the assessment of NAFLD.

2 Methods

2.1 *Experimental Setup*

Both *in vivo* and *ex vivo* PAI were performed in this study. Before photoacoustic (PA) scanning, the anatomical regions of interest are scanned using an ultrasound system with a linear array working at 8.5 MHz, 100 Hz frame rate (iNSIGHT 23R, Saset Healthcare, Inc. Chengdu, China) by a single professional operator. The setup for *in vivo* PA imaging [Fig. 1(a)] is based on a *Q*-switched Nd:YAG-pumped optical parameter oscillator (Surelite, Continuum, California), a 128-element concave ultrasound transducer array (Japan Probe Corporation, Yokohama, Japan), and a 64-channel DAQ system (PXIe5105, National Instrument, USA). The diameter of the array is 100 mm. The pitch size of each element is 2 mm. The laser provides tunable laser pulses from 700 to 960 nm at a repetition rate of up to 20 Hz. The output laser light is coupled into a custom-made fiber bundle. The output shape of the fiber bundle is a rectangular region with a 10 mm × 5 mm area. The maximum light fluence from the fiber bundle at 800 nm is estimated to be 13.6 mJ/cm^2 (within the safety limit of the American National Standards Institute regulations). The concave ultrasound transducer array has a center frequency of 5 MHz (~90% two-way

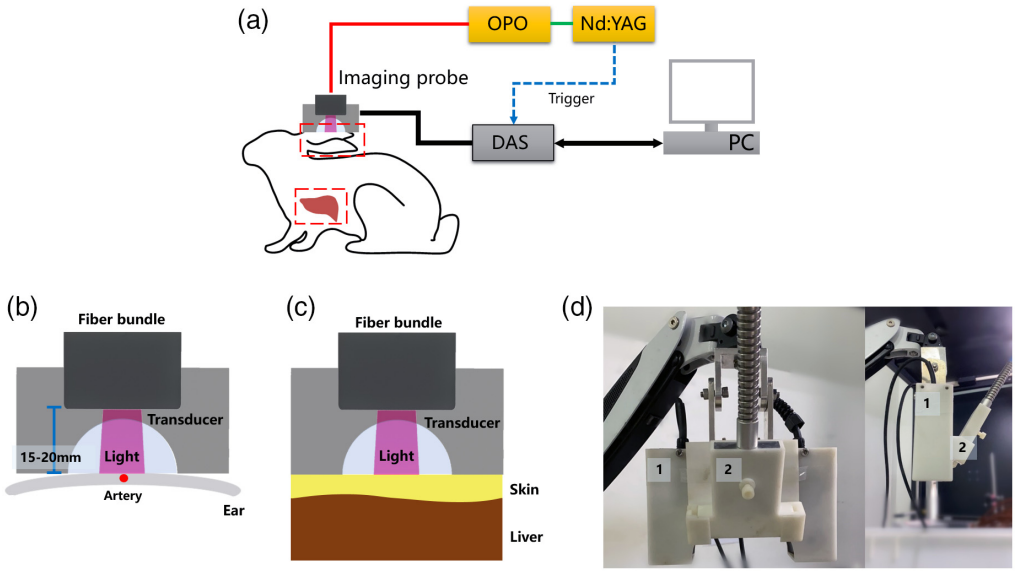

Fig. 1 A schematic of the *in vivo* PAI experimental system. (a) The hardware components employed in the PAI system. (b), (c) Schematics showing two *in vivo* imaging positions at the central artery on the ear and liver, respectively. (d) Photograph of the PA probe: (1) ultrasound transducer and (2) fiber bundles. DAS, data acquisition system (preamplifiers, multiplexers, and analog-to-digital converters); Nd:YAG, Nd:YAG pumping laser; OPO, optical parameter oscillator system; PC, personal computer; and imaging probe, a 128-element transducer array, a fiber bundle, and a resin shell enclosed with a membrane.

relative bandwidth) with about 2.1 mm in radius one-way Nyquist zone[30,31] and a spatial resolution of ∼150 μm for cross-sectional imaging. The array is enclosed with a resin shell covered by a membrane (100-μm thickness), and water is filled into the space between the membrane and transducer. In the animal study, the PAI probe was put on the animal body (ear or skin surface), and the fiber bundle output was adjusted so that the illumination area was right at the center of the transducer [about 25 deg illumination angle, 15 to 20 mm height as shown in Figs. 1(b) and 1(c)].

Detected PA signals are amplified through a custom-built low-noise preamplifier (55 dB) and transferred to a 64-channel analog-to-digital system (PXIe5105, National Instrument, Texas) after 2:1 multiplexing with 12-bit digital resolution and 50 MS/s sampling rate. Thus the frame rate of the system is 10 Hz. Signals are saved in the onboard computer (PXIe8840, National Instruments, Texas, USA) which also works as a control panel for the PAI system.

The setup for the *ex vivo* PA imaging is adapted from the *in vivo* system, as illustrated in Fig. 2(a). The output laser light is coupled into a custom-made fiber bundle to illuminate the whole area of a sample from the above, achieving an averaged light fluence of 13.6 mJ/cm^2 on

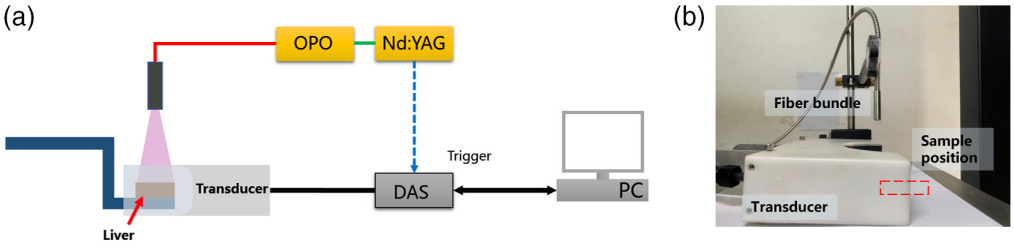

Fig. 2 (a) The hardware components employed in *ex vivo* experiments. (b) Picture of the PA probe. DAS, data acquisition system (preamplifiers, multiplexers, and analog-to-digital converters); OPO, optical parameter oscillator system; PC, personal computer; and Nd:YAG, Nd:YAG bumping laser.

the sample surface at 800 nm (again within the safety limit of the American National Standards Institute regulations). A sample piece is cut from an intact lobe of a rabbit liver with a thickness of 1 to 2 mm. The same concave ultrasound transducer array is used to perform 2D tomographic imaging of an *ex vivo* liver. Both the tissue and transducer are put in a small water tank. The liver tissue is fixed in a cylindrical sample holder made from resin and put in the center of the transducer to ensure maximum ultrasound sensitivity and the laser beam from the fiber was 15 mm above the tissue to produce a rounded area of illumination [Fig. 2(b), water tank and sample holder is not shown here]. After amplification by our custom-built preamplifier, the PA signal is recorded with the DAQ system.

2.2 *Animal Model Preparation*

New Zealand rabbits ($n = 11$, male, weight: 2.5 to 2.7 kg) were used in this study. The NAFLD group ($n = 8$) was fed with a standard diet for the first 8 weeks, followed by a high-fat diet (75% standard feed with 10% butter, 2% cholesterol, 5% sugar, and 8% yolk powder) for the 12 weeks thereafter. The control group ($n = 3$) was fed with the standard diet (100% standard feed) for 20 weeks.[32] These diets were provided by Dashuo Laboratory Animal Co., LTD, Chengdu, China.

2.3 *In Vivo LFR Assessment*

For the *in vivo* LFR assessment, 11 rabbits in two groups underwent PAI scanning of the liver region and ICG injection. All the animals were first anesthetized by isoflurane gas inhalation and were put on a warming pad and fixed to a custom-made animal pad to set in the right lateral position. We first used traditional ultrasonic imaging (US) to find the left lateral lobe of the liver for reference. The PA imaging probe was then placed at the same position as the US probe to acquire PA images, as shown in Fig. 1(c). Posture and imaging probe placements (both US and PA) were standardized and marked to ensure scanning reproducibility.

For *in vivo* imaging, multispectral PA signals were acquired at 760, 800, 850, and 930 nm to obtain oxygenated hemoglobin (HbO_2), deoxygenated hemoglobin (HbR), and lipid according to previous studies.[21] Twenty images were continuously acquired at one wavelength without averaging. After the multispectral imaging, the PAT imaging probe was placed above the right central auricular artery (CAA) as shown in Fig. 1(b) and the ICG was injected through the left auricular vein. Corresponding US images were acquired at the same position.

Before the PAI scan, ICG was dissolved in distilled water to obtain a concentration of 5 mg/ml. PAI scanning at 805 nm was performed for 20 min over the right CAA. The acquisition rate was 1 frame per second (time-averaged for 10 consecutive frames). One minute after a baseline PAI scan, a dose of 0.1 ml/kg ICG solution was injected via the left auricular vein along with a 5-ml saline flush for 10 s. Then the PA signal was continuously acquired for additional 19 min.

2.4 *Ex Vivo and Histological Examination*

After the *in vivo* imaging examination, representative tissue specimens were taken from previously imaged anatomical regions. After harvesting, tissue specimens from the same lobe were divided into two parts, one for *ex vivo* PA imaging, and the other one was fixed in a 4% formaldehyde/PBS solution and then embedded in paraffin.

For the *ex vivo* experiments, multispectral PA signals were acquired at 760, 800, 850, and 930 nm. For histological examination, liver tissue sections were stained with haematoxylin–eosin (HE) and Masson. The histologic features were evaluated with the NAFLD activity score (NAS), which was calculated as the unweighted sum of the scores for steatosis (0 to 3), lobular inflammation (0 to 3), and ballooning (0 to 2). Based on the NAS score, NAFLD was classified as "NAFLD but not-NASH" (NAS < 3), "borderline-NASH" (NASH = 3 to 4), and "definite-NASH" (NAS = 5 to 8). The classification process was performed by a pathologist with 8 years of experience in liver histology, who was blinded to the PA results.

To estimate the lipid area in H&E staining images, we used a machine learning toolbox (WeKa3)[33] in Fiji (National Institutes of Health). One expert labeled H&E staining images

at NAS = 3 which have a large area of lipid cells to train the network. Then the trained network was applied to classify all slices then the area of lipid cells was segmented by setting a threshold. The results were shown using the lipid cells area divided by the total area of the image.

2.5 *Image Reconstruction and Spectral Unmixing*

PA images were first reconstructed in Labview (National Instruments, USA) in real time using a back-projection algorithm[34] with real-time display. The raw PA data were also stored for offline processing by MATLAB (R2016b, Mathworks, Inc., MA, USA). In the offline processing, 0.2 to 10 MHz filtering was applied to remove high-frequency noise, and then PA images were reconstructed offline using back-projection schemes.[35]

To remove the breathing-related artifact, we built a MATLAB code as described previously.[36] Briefly, after we got 20 frames (each frame obtained without averaging) from one wavelength, a correlation coefficient (CC) was calculated among these frames. Frames with movement showing significantly low CC (slight movement: 0.9 to 1, breathing: 0.5 to 0.7) were rejected. In most cases, about 12 to 14 frames were effective and averaged as one wavelength image. We then repeated the same process above for different wavelengths and registered all averaged images to that for the first wavelength for spectral unmixing.

A linear unmixing was applied to obtain the signal from three endogenous absorbers following previous studies,[21,37] and then values of HbR, HbO_2, and lipid were obtained. Lipid unmixing was based on all wavelengths (760, 800, 850, and 930 nm), whereas the HbR and HbO_2 signals were calculated from a subrange (760, 800, and 850 nm), which is more accurate in unmixing due to increased water absorptivity at higher wavelengths.[38] The total hemoglobin (HbT = HbR + HbO_2) and lipid values were calculated from 4 mm × 2 mm (long × width) regions of interest close to the surface of the skin to minimize error due to the linear unmixing.[39] The averaged HbT signal, HbT_{mean}, lipid signal, and $lipid_{mean}$ were calculated for statistical analysis.

To minimize the error from unknown light fluence, we first measured the laser energy below the imaging probe and normalized the energy among different wavelengths. Then we divided our image into two parts, skin and liver based on the clear structural differences in PA images and referred to corresponding US images. A depth compensation method based on recently published research was applied to each wavelength[40] for *in vivo* data. The relevant optical parameters were obtained from two other papers.[41,42] For *ex vivo* data, we measured the laser energy on the tissue surface and normalize the energy. Since only the liver tissues were imaged in 2D form. No depth compensation was applied.

2.6 *Statistical Analysis*

Statistical analysis and graphical display of data were performed using GraphPad software (version 7.00; GraphPad Software, San Diego, CA, USA). In the ICG results, continuous variables were given as means and SEM in the manually selected ROI region at the CAA. Continuous PA images were registered to the first frame. Similar to the previous study,[29] averaged PA signals in the CAA were normalized as the relative PA signal intensity (PSI_{re}) to reflect the ICG concentration change as follows:

$$\mathrm{PSI}_{\mathrm{re}}(t) = \frac{\mathrm{PSI}(t) - \mathrm{PSI}_{\mathrm{base}}}{\mathrm{PSI}_{\mathrm{base}}}.$$

$\mathrm{PSI}_{\mathrm{base}}$ is the base PSI before ICG injection which is generated from hemoglobin. $\mathrm{PSI}(t)$ is the PSI at time t. To quantify the kinetics of $\mathrm{PSI}_{\mathrm{re}}$ change after the ICG injection, an exponential decay model[43] was used as follows:

$$\mathrm{PSI}_{\mathrm{re}}(t) = \mathrm{PSI}_{\mathrm{re}}(0)e^{-kt},$$

where the elimination time (t_0) indicates the elapsed time from $\mathrm{PSI}_{\mathrm{re}}(0)$ to the baseline. The rate constant (k) gives the decay rate.

A mean total hemoglobin (HbT_{mean}) and lipid signal ($lipid_{mean}$) were calculated over anatomical regions. *In vivo* and *ex vivo* statistical analyses between two groups (NAFLD versus

control) of PA parameters and histological results were conducted using independent samples t-tests. A value of $p < 0.05$ was considered statistically significant. The correlation between *in vivo* and *ex vivo* lipid signals, between lipid signal and lipid/unit area, were calculated using linear regression.

3 Results

3.1 *In Vivo ICG Clearance Studies*

ICG clearance studies were conducted first by real-time PAI for both groups (NAFLD and control group). PAI and US sections of the CAA *in vivo* were displayed as the region of interest (ROI) in Fig. 3(a) (top and bottom panels, respectively) (yellow dashed circle and arrow). Figure 3(c) shows the *in vivo* ICG measurements from the CAA. The CCA can be found easily in both the PA and US images. After the injection of ICG at the 60-s time point, a high-intensity peak was observed and gradually decreased over time [Fig. 3(c)]. Statistical results for k display a high value in the control group and a lower value in the lipid group. The time to recovery also showed significant differences between the two groups.

The control group showed a rapid decrease after the peak point, whereas the elimination of ICG for the NAFLD group was slower [Fig. 3(c)]. Two major parameters were analyzed here. We calculated k to show a difference in elimination rate (k_1 versus k_2, 0.0192 ± 0.0029 versus 0.00422 ± 0.0023, $P < 0.0001$). In addition, the elimination time (t_0), which indicates the elapsed time after the summit of the injection to the baseline, was also analyzed (t_{01} versus t_{02}, 174.7 ± 33.50 s versus 661.5 ± 131.2 s, $P = 0.0002$).

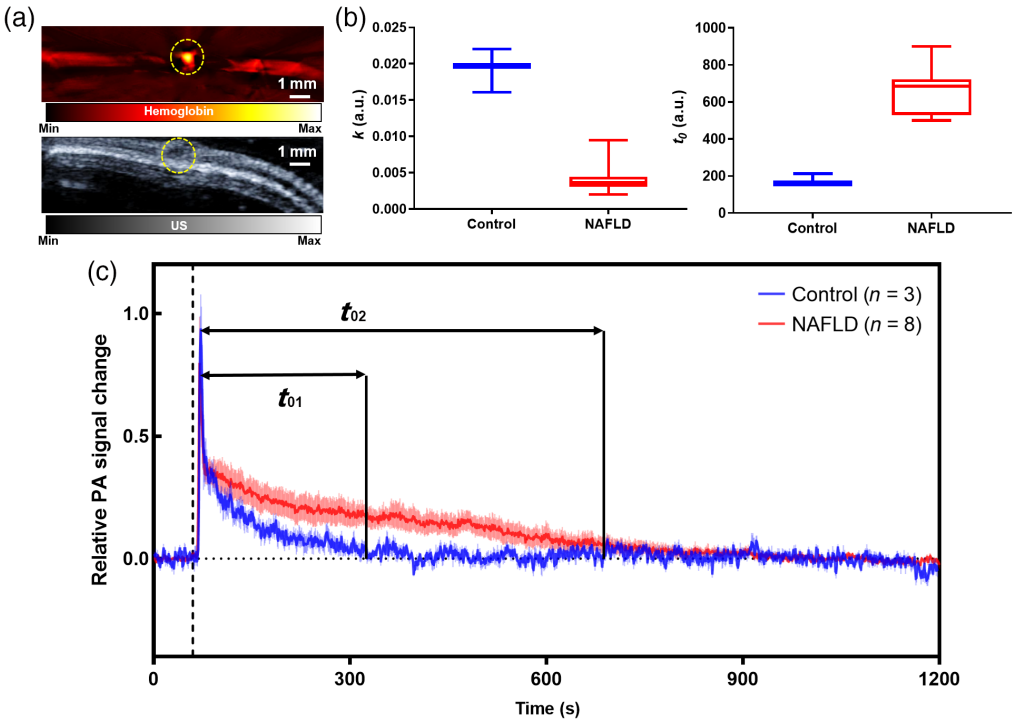

Fig. 3 ICG clearance studies between NAFLD and control groups of rabbits (NAFLD, $n = 8$ and control group, $n = 3$). (a) Transverse PA (top) and US (bottom) images of the rabbit ear with the CAA (yellow dashed circle). ROI (yellow dashed circle) was selected to determine the PA signal intensity. (b) The elimination rate constant k (left) and elimination time t_0 (right). (c) Temporal PA signal trace from 11 rabbits in two groups. For each curve, data were normalized to the highest intensity acquired.

3.2 *Lipid Detection in a NAFLD Model*

ICG clearance can serve as a biomarker for liver function but cannot provide lipid content, critical for accessing NAFLD. Hence, following the ICG clearance studies, multispectral PA studies were conducted.

US and PA imaging was performed in NAFLD rabbits and the control group. Spectral unmixing was applied to obtain HbT_{mean} and lipid images [Figs. 4(a) and 4(b)]. From the PA images, distinguishable features are present, indicating different tissue types around the liver. High HbT_{mean} value regions reveal vascular-rich tissue areas, the dermal layer, and liver vessels. The high lipid signal regions were the subcutaneous lipid and liver. Due to the spectral unmixing, we can find significant differences in lipid concentration across the liver.

To select the ROI in the liver region for analysis, ultrasound images were used as a guide to ensure the liver's location. Then the HbT_{mean} images showed distinguishable features which helped us to find the liver region below the skin layer and superficial vessels. Moreover, due to the limitation of our linear unmixing method,[39] a rectangle region was selected close to the top of the liver to calculate the mean lipid values ($lipid_{mean}$) and lipid/HbT ratio ($lipid_{mean}/HbT_{mean}$) in this region.

A significant difference in the $lipid_{mean}$ value was observed ($lipid_{mean} = 0.081 \pm 0.0161$ arbitrary units (a.u.) control versus NAFLD 0.198 ± 0.048 a.u., $P = 0.003$). Second, when comparing total hemoglobin between control and NAFLD groups ($HbT_{mean} = 0.857 \pm 0.104$ a.u. versus 0.95 ± 0.40 a.u., $P = 0.410$), no significant difference was found. The lipid to hemoglobin ratio per independent rabbit between groups was also computed ($lipid_{mean}/HbT_{mean} = 0.101 \pm 0.018$ a.u. versus 0.218 ± 0.072 a.u., $P = 0.0255$) and a showed significant difference.

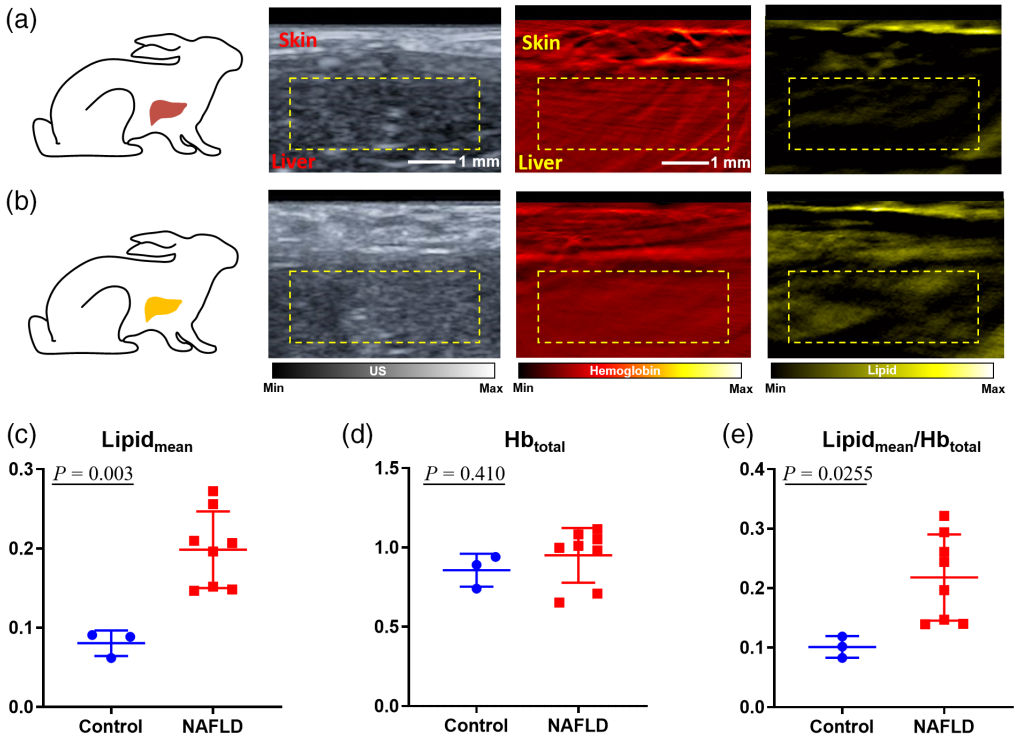

Fig. 4 *In vivo* PA imaging: representative images of liver from (a) healthy and (b) NAFLD rabbits. ROIs (yellow boxes) are determined in the US images for analysis. The PA/US images show HbT_{mean} and lipid distributions within the liver and ROI, respectively. Differences in spectrally unmixed PA images between healthy and NAFLD rabbits are shown. (c), (e) $Lipid_{mean}$ as well as $lipid_{mean}/HbT_{mean}$ for healthy and NAFLD rabbits. Each blue-filled circle and red-filled cube represents the mean PA signal per independent liver region for the healthy and NAFLD rabbits, respectively.

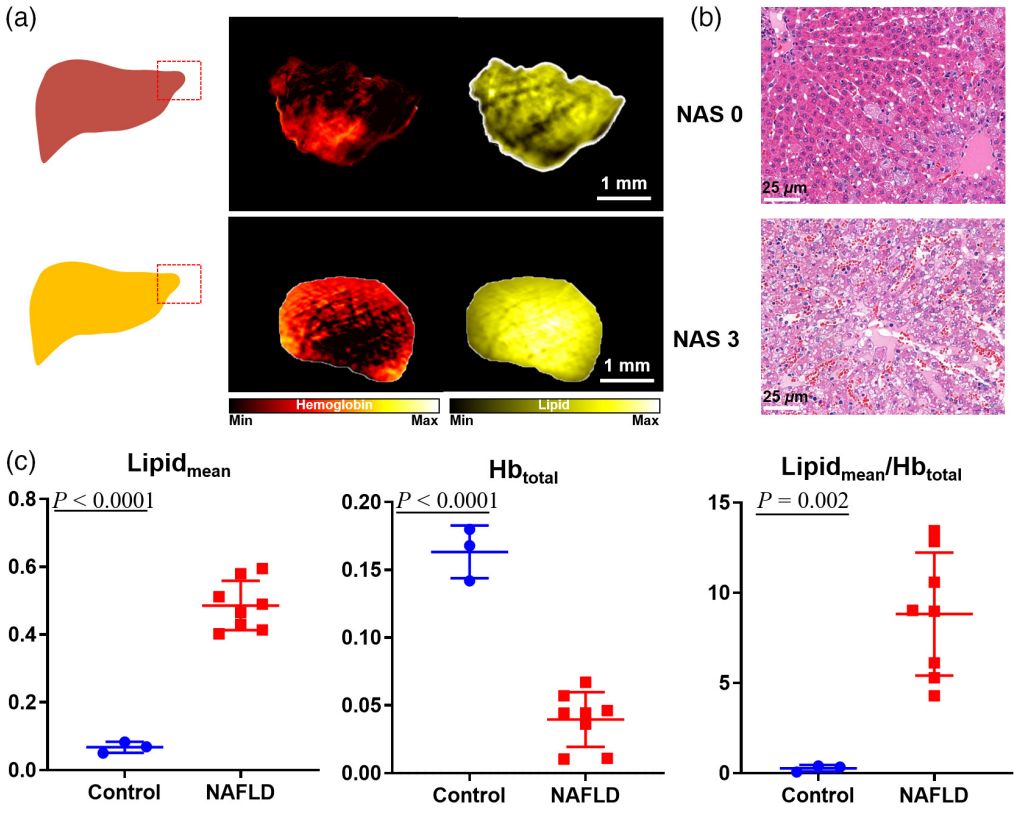

Fig. 5 *Ex vivo* PA imaging from liver samples (control = 3 and NAFLD = 8). (a) Representative images of liver samples for healthy (upper row) and NAFLD (bottom row) rabbits. Averaged PA signals, HbT_{mean}, and lipid distribution were calculated based on a small sample from the whole liver (red dashed line), respectively. Differences in spectrally unmixed PA images between healthy and NAFLD rabbits are shown. (b) Representative H&E staining for the control group (upper row) and NAFLD group (bottom row) from corresponding liver tissue. (c) $Lipid_{mean}$ as well as $lipid_{mean}/HbT_{mean}$ for the healthy and NAFLD rabbits. Each blue-filled circle and red-filled cube represents the mean PA signal per independent liver region for the healthy and NAFLD rabbits, respectively.

3.3 *Ex Vivo Fatty Liver Imaging*

To verify the *in vivo* findings, corresponding tissue specimens were taken from both groups. Representative PA images of HbT_{mean} and lipid were shown in Fig. 5(a) and corresponding histological results were shown in Fig. 5(b). Similar to *in vivo* analysis, mean lipid values ($lipid_{mean}$) and lipid/HbT ratio ($lipid_{mean}/HbT_{mean}$) were compared between two groups. First, a significant difference in $lipid_{mean}$ was observed ($lipid_{mean} = 0.0673 \pm 0.0165$ versus 0.486 ± 0.073 a.u., $P < 0.0001$). Second, a significant difference was also seen in total hemoglobin between the two groups ($HbT_{mean} = 0.163 \pm 0.0194$ versus 0.0396 ± 0.0201 a.u., $P < 0.0001$). Finally, lipid/HbT ratio showed a significant difference between the two groups ($lipid_{mean} = 0.273 \pm 0.179$ versus 8.82 ± 3.40 a.u., $P = 0.002$).

3.4 *Relationship Between PA Signal and Histology*

We also compared the PA signal (i.e., $lipid_{mean}$) with histopathological classification. The details of the histopathological scores on steatosis (0 to 3), lobular inflammation (0 to 3), and ballooning (0 to 2) of each rabbit are shown in Table 1. Based on the NAS score, NAFLD group rabbits were classified as "NAFLD but not-NASH" (NAS < 3), "borderline-NASH" (NASH = 3 to 4), and "definite-NASH" (NAS = 5 to 8).

As shown in Fig. 6(a), there was a progressive elevation in the *in vivo* $lipid_{mean}$ with increased severity from not-NASH to borderline-NASH. There was a significant difference in $lipid_{mean}$

Table 1 Detailed histopathological scores and PA values NAFLD rabbits and control group (C1 to C3).

Number	Steatosis (0 to 3)	Lobular inflammation (0 to 3)	Hepatocellular ballooning (0 to 3)	PA *in vivo* $\text{lipid}_{\text{mean}}$ (a.u.)	PA *ex vivo* $\text{lipid}_{\text{mean}}$ (a.u.)
1	1	0	0	0.1963	0.430
2	1	0	2	0.2724	0.5959
3	1	1	2	0.2099	0.512
4	1	1	1	0.2068	0.5841
5	1	1	2	0.2562	0.49
6	1	0	1	0.1467	0.4142
7	1	0	1	0.1518	0.4025
8	1	0	0	0.1485	0.465
C1	0	0	0	0.08	0.08
C2	0	0	0	0.062	0.05
C3	0	0	0	0.091	0.069

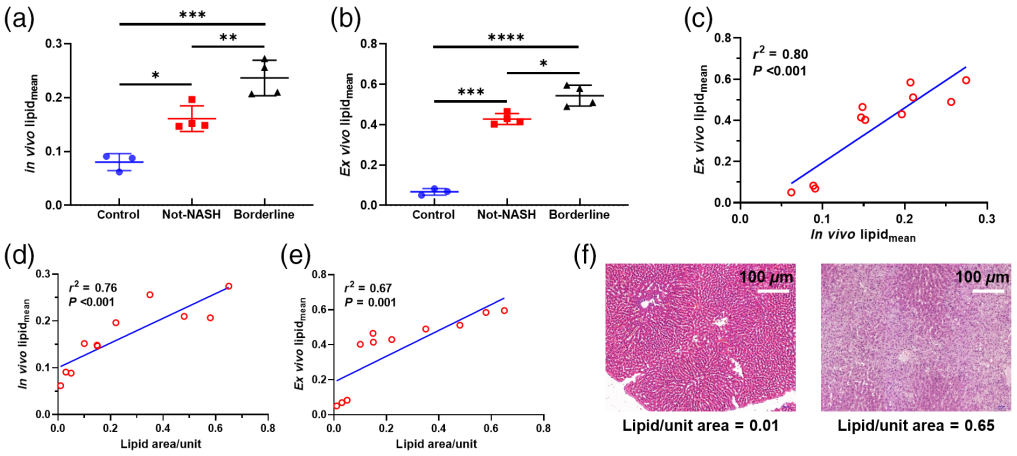

Fig. 6 Scatter plots of the comparisons between PA signal and histopathological results. (a) *In vivo* quantitative assessment of steatosis by PAI in comparison to histological grading. Control: $n = 3$; not-NASH: $n = 4$; and borderline: $n = 4$. (b). *Ex vivo* quantitative assessment of steatosis by PA in comparison to histological grading. (c). Linear regression between *ex vivo* and *in vivo* lipid data. (d) *In vivo* quantitative assessment of lipid by PAI in comparison to histological estimates. (e) *Ex vivo* quantitative assessment of lipid by PAI in comparison to histological estimates. (f) Representative H&E staining for the control group (left) and NAFLD group (right) from corresponding liver tissue.

between control and not-NASH (0.0802 ± 0.0159 versus 0.160 ± 0.0237 a.u. $P = 0.04$). The $\text{lipid}_{\text{mean}}$ increased significantly in borderline-NASH groups and showed significant differences between not-NASH and borderline-NASH (0.160 ± 0.0237 versus 0.236 ± 0.033 a.u. $P = 0.009$). Significant differences were also shown between control and borderline-NASH (0.0802 ± 0.0159 versus 0.236 ± 0.033 a.u., $P = 0.0007$).

In the *ex vivo* results, significant differences in $\text{lipid}_{\text{mean}}$ were shown between control and not-NASH (0.0673 ± 0.0166 versus 0.395 ± 0.0691 a.u. $P = 0.0001$). As the $\text{lipid}_{\text{mean}}$ increased,

significant differences were shown between control and borderline-NASH (0.06733 ± 0.01656 versus 0.544 ± 0.0518 a.u. $P = 0.0109$). The $\text{lipid}_{\text{mean}}$ between not-NASH and borderline-NASH also showed significant differences (0.395 ± 0.0691 versus 0.544 ± 0.0518 a.u. $P = 0.0109$).

According to data in Table 1, the linear regression between *ex vivo* and *in vivo* lipid data is shown in Fig. 6(c) ($r^2 = 0.80$, $P < 0.001$).

To evaluate the correlation between PA lipid estimation and the histology estimates, we calculated the relative area of lipid/unit area in each staining slice. Figures 6(d) and 6(e) showed that lipid value from PA images has a relatively high correlation with the lipid area. *In vivo* mean lipid values ($\text{lipid}_{\text{mean}}$) had a good correlation with histology estimates ($r^2 = 0.76$, $P < 0.001$), and *ex vivo* $\text{lipid}_{\text{mean}}$ were well correlated with histology estimates ($r^2 = 0.67$, $P < 0.001$). The H&E staining images showed normal hepatic tissue and steatosis pathology.

4 Discussion and Conclusion

In our previous work, we demonstrated the capability of PAI-based ICG clearance for LFR assessment in rabbits,[29] the accuracy of which was confirmed by the gold standard method spectrophotometry. In this work, we applied PAI/ICG to assess LFR in rabbits with NAFLD. We have shown that time-resolved PA signal can differentiate the kinetics of ICG uptake and excretion in control and NAFLD groups *in vivo*, indicating LFR impairment occurred during the development process of NAFLD.

Although hepatic ICG clearance serves as a biomarker for liver function in the assessment of NAFLD rabbit, NAFLD cannot be quantified by it. The pathology of NAFLD is a spectrum of lesions ranging from pure steatosis to a complex pattern with significant necroinflammatory injury, fibrosis, or even cirrhosis.[44] Therefore, LFR assessment was necessary but not enough for the diagnosis and treatment of the pathological change of NAFLD.

Multispectral PAI is a target-specific, quantitative, noninvasive, imaging modality[38] when compared with established imaging modalities, including ultrasound imaging and MRI. To obtain more specific information about NAFLD liver, *in vivo* and *ex vivo* multispectral PAI were performed and the results from our study demonstrated a significant increase in lipid content in the liver of the NAFLD group compared to the control group, which agreed well with the pathologic results, indicating lipid metabolism malfunction in the NAFLD liver tissue.[26,45] Both *in vivo* and *ex vivo* mean lipid values displayed a high correlation with histology estimates, which indicated the accuracy of using PAT for steatosis assessment of NAFLD. This was in line with previous studies in mice of NAFLD.[27,46] In addition, the linear correlation between lipid *in vivo* and *ex vivo* mean lipid is also relatively high.

The divergent outcomes for the *in vivo* and *ex vivo* HbT results may come from several reasons. First, the liver has a strong HbT_{mean} signal as it is a vascular-rich tissue and HbT_{mean} stands for strong endogenous absorbers *in vivo*. In an *ex vivo* setting, HbT_{mean} signal decreased drastically due to blood loss in the tissue. In general, pathological changes associated with steatosis could be unequivocally detected using multispectral PAI both *in vivo* and *ex vivo*, consistent with similar findings from recent studies in mice.[46]

In addition, the pathological changes in those two situations (*in vivo* and *ex vivo*), we note that there are some limitations in our current study. The light absorption of lipid in the 760- to 930-nm range is much weaker than that at 1200 and 1720 nm which might be a better wavelength to detect lipid regions.[47] As the limitation of our laser system, output energy at 1200 and 1720 nm is too low for PA imaging. As an alternative method, we refer to previous research[21,38] to use 930 nm and other wavelengths (e.g., 760, 800, 850, and 930 nm). Those wavelengths with some water absorption may induce inconsistent lipid areas as shown in Fig. 4(b) and show some "patchy" in the NAFLD liver.

Although we have a good correlation between PA lipid value and histology lipid area, we should notice that the r^2 is below 0.9 and more studies are needed. For example, we can briefly calculate the lipid area in H&E staining and compare it with our PA image results. Red oil O staining will be a better choice to estimate the lipid area. In addition, we need to optimize our system settings including the illumination geometry and fiber bundle parameters in both *in vivo* and *ex vivo* setups.

Except for the hardware, since we applied zero-thresholding to remove the negative signals in figures, some artifacts in reconstructed images may affect the quantitative results.[48] A recently developed method based on Hilbert transformation can be applied in the future to remove such noise and give more strict quantitative measurements.[31,48] In addition, the linear unmixing method may be another reason which affects our results. Advanced spectral unmixing methods[21,49] need to be developed to achieve the capability of refined quantification of PA signal.

In sum, this study showed significantly injured LFR in the NAFLD group compared to the control group. A future study with a larger sample size is needed to investigate the LFR change during various NAFLD pathologies. Due to the limitation of the sample size used in this study, refined PA classification of the NAFLD is not achieved. We are developing an advanced NAFLD animal model with various pathology states and upgrading our PAI system for this challenging study.

Disclosures

The authors declare no conflicts of interest.

Acknowledgment

This study was supported by the National Natural Science Foundation of China (NSFC) (Grant No. 82001833) and the Post-Doctor Research Project, West China Hospital, Sichuan University (Grant No. 2019HXBH014).

Code, Data, and Materials Availability

Data used in the research can be made available to obtain the results reported in the article; please contact the corresponding author.

References

1. Q. M. Anstee, D. Seth, and C. P. Day, "Genetic factors that affect risk of alcoholic and nonalcoholic fatty liver disease," *Gastroenterology* **150**(8), 1728–1744.e7 (2016).
2. P. S. Dulai, C. B. Sirlin, and R. Loomba, "MRI and MRE for non-invasive quantitative assessment of hepatic steatosis and fibrosis in NAFLD and NASH: clinical trials to clinical practice," *J. Hepatol.* **65**(5), 1006–1016 (2016).
3. Z. M. Younossi et al., "Global epidemiology of nonalcoholic fatty liver disease—meta-analytic assessment of prevalence, incidence, and outcomes," *Hepatology* **64**(1), 73–84 (2016).
4. EASL-EASD-EASO, "Clinical practice guidelines for the management of non-alcoholic fatty liver disease," *Obesity Facts* **9**(2), 65–90 (2016).
5. V. Ratziu et al., "Sampling variability of liver biopsy in nonalcoholic fatty liver disease," *Gastroenterology* **128**(7), 1898–1906 (2005).
6. Z. M. Younossi et al., "Nonalcoholic fatty liver disease: assessment of variability in pathologic interpretations," *Mod. Pathol.* **11**(6), 560–565 (1998).
7. Z. M. Younossi, "Long-term outcomes of nonalcoholic fatty liver disease: from non-alcoholic steatohepatitis to nonalcoholic steatofibrosis," *Clin. Gastroenterol. Hepatol.* **15**(8), 1144–1147 (2017).
8. L. Castera, V. Vilgrain, and P. Angulo, "Noninvasive evaluation of NAFLD," *Nat. Rev. Gastroenterol. Hepatol.* **10**(11), 666–675 (2013).
9. Z. Permutt et al., "Correlation between liver histology and novel magnetic resonance imaging in adult patients with non-alcoholic fatty liver disease – MRI accurately quantifies hepatic steatosis in NAFLD," *Alimentary Pharmacol. Ther.* **36**(1), 22–29 (2012).
10. M. Noureddin et al., "Utility of magnetic resonance imaging versus histology for quantifying changes in liver fat in nonalcoholic fatty liver disease trials," *Hepatology* **58**(6), 1930–1940 (2013).

11. C. C. Park et al., "Magnetic resonance elastography vs transient elastography in detection of fibrosis and noninvasive measurement of steatosis in patients with biopsy-proven nonalcoholic fatty liver disease," *Gastroenterology* **152**(3), 598–607.e2 (2017).
12. K. Okubo et al., "Visualization of quantitative lipid distribution in mouse liver through near-infrared hyperspectral imaging," *Biomed. Opt. Express* **12**(2), 823–835 (2021).
13. L. Castera, M. Friedrich-Rust, and R. Loomba, "Noninvasive assessment of liver disease in patients with nonalcoholic fatty liver disease," *Gastroenterology* **156**(5), 1264–1281.e4 (2019).
14. H. Imamura et al., "Assessment of hepatic reserve for indication of hepatic resection: decision tree incorporating indocyanine green test," *J. Hepato-Biliary-Pancreatic Surg.* **12**(1), 16–22 (2005).
15. Y.-Y. Wang et al., "Comparison of the ability of Child-Pugh score, MELD score, and ICG-R15 to assess preoperative hepatic functional reserve in patients with hepatocellular carcinoma," *J. Surg. Oncol.* **118**(3), 440–445 (2018).
16. Q. Liu et al., "Lipid metabolism and functional assessment of discarded human livers with steatosis undergoing 24 hours of normothermic machine perfusion," *Liver Transplant.* **24**(2), 233–245 (2018).
17. A. Becker et al., "Multispectral optoacoustic tomography of the human breast: characterisation of healthy tissue and malignant lesions using a hybrid ultrasound-optoacoustic approach," *Eur. Radiol.* **28**(2), 602–609 (2018).
18. M. Yang et al., "Photoacoustic/ultrasound dual imaging of human thyroid cancers: an initial clinical study," *Biomed. Opt. Express* **8**(7), 3449–3457 (2017).
19. J. R. Rajian et al., "Characterization and treatment monitoring of inflammatory arthritis by photoacoustic imaging: a study on adjuvant-induced arthritis rat model," *Biomed. Opt. Express* **4**(6), 900–908 (2013).
20. F. Knieling et al., "Multispectral optoacoustic tomography for assessment of Crohn's disease activity," *N. Engl. J. Med.* **376**(13), 1292–1294 (2017).
21. G. Diot et al., "Multispectral optoacoustic tomography (MSOT) of human breast cancer," *Clin. Cancer Res.* **23**(22), 6912 (2017).
22. L. V. Wang and S. Hu, "Photoacoustic tomography: in vivo imaging from organelles to organs," *Science* **335**(6075), 1458 (2012).
23. X. Shu et al., "Quantifying melanin concentration in retinal pigment epithelium using broadband photoacoustic microscopy," *Biomed. Opt. Express* **8**(6), 2851–2865 (2017).
24. G. S. Sangha, E. H. Phillips, and C. J. Goergen, "In vivo photoacoustic lipid imaging in mice using the second near-infrared window," *Biomed. Opt. Express* **8**(2), 736–742 (2017).
25. Y. Yan et al., "Photoacoustic imaging of the uterine cervix to assess collagen and water content changes in murine pregnancy," *Biomed. Opt. Express* **10**(9), 4643–4655 (2019).
26. G. Xu et al., "The functional pitch of an organ: quantification of tissue texture with photoacoustic spectrum analysis," *Radiology* **271**(1), 248–254 (2014).
27. O. Rom et al., "Nitro-fatty acids protect against steatosis and fibrosis during development of nonalcoholic fatty liver disease in mice," *EBioMedicine* **41**, 62–72 (2019).
28. C. Tian et al., "Imaging and sensing based on dual-pulse nonlinear photoacoustic contrast: a preliminary study on fatty liver," *Opt. Lett.* **40**(10), 2253–2256 (2015).
29. T. Qiu et al., "Assessment of liver function reserve by photoacoustic tomography: a feasibility study," *Biomed. Opt. Express* **11**(7), 3985–3995 (2020).
30. P. Hu et al., "Spatiotemporal antialiasing in photoacoustic computed tomography," *IEEE Trans. Med. Imaging* **39**(11), 3535–3547 (2020).
31. L. Li et al., "Single-impulse panoramic photoacoustic computed tomography of small-animal whole-body dynamics at high spatiotemporal resolution," *Nat. Biomed. Eng.* **1**(5), 0071 (2017).
32. M. A. Van Herck, L. Vonghia, and S. M. Francque, "Animal models of nonalcoholic fatty liver disease—a starter's guide," *Nutrients* **9**(10), 1072 (2017).
33. M. Hall et al., "The WEKA data mining software: an update," *ACM SIGKDD Explor. Newslett.* **11**(1), 10–18 (2009).
34. M. Xu and L. V. Wang, "Universal back-projection algorithm for photoacoustic computed tomography," *Phys. Rev. E* **71**(1), 016706 (2005).

35. J. Yang et al., "Photoacoustic assessment of hemodynamic changes in foot vessels," *J. Biophotonics* **12**(6), e201900004 (2019).
36. T. F. Fehm et al., "In vivo whole-body optoacoustic scanner with real-time volumetric imaging capacity," *Optica* **3**(11), 1153–1159 (2016).
37. V. Ntziachristos and D. Razansky, "Molecular imaging by means of multispectral optoacoustic tomography (MSOT)," *Chem. Rev.* **110**(5), 2783–2794 (2010).
38. A. P. Regensburger et al., "Detection of collagens by multispectral optoacoustic tomography as an imaging biomarker for Duchenne muscular dystrophy," *Nat. Med.* **25**(12), 1905–1915 (2019).
39. H. Roman et al., "Estimating blood oxygenation from photoacoustic images: can a simple linear spectroscopic inversion ever work?" *J. Biomed. Opt.* **24**(12), 121914 (2019).
40. S. Park et al., "Normalization of optical fluence distribution for three-dimensional functional optoacoustic tomography of the breast," *J. Biomed. Opt.* **27**(3), 036001 (2022).
41. P. Parsa, S. L. Jacques, and N. S. Nishioka, "Optical properties of rat liver between 350 and 2200 nm," *Appl. Opt.* **28**(12), 2325–2330 (1989).
42. S. Kumari and A. K. Nirala, "Study of light propagation in human, rabbit and rat liver tissue by Monte Carlo simulation," *Optik* **122**(9), 807–810 (2011).
43. N. Brillant et al., "Dynamic and accurate assessment of acetaminophen-induced hepatotoxicity by integrated photoacoustic imaging and mechanistic biomarkers in vivo," *Toxicol. Appl. Pharmacol.* **332**, 64–74 (2017).
44. S. L. Friedman et al., "Mechanisms of NAFLD development and therapeutic strategies," *Nat. Med.* **24**(7), 908–922 (2018).
45. K. Pei et al., "An overview of lipid metabolism and nonalcoholic fatty liver disease," *BioMed. Res. Int.* **2020**, 4020249 (2020).
46. S. Huang et al., "Functional multispectral optoacoustic tomography imaging of hepatic steatosis development in mice," *EMBO Mol. Med.* **13**, e13490 (2021).
47. T. Allen et al., "Spectroscopic photoacoustic imaging of lipid-rich plaques in the human aorta in the 740 to 1400 nm wavelength range," *J. Biomed. Opt.* **17**(6), 061209 (2012).
48. G. Li et al., "Multiview Hilbert transformation for full-view photoacoustic computed tomography using a linear array," *J. Biomed. Opt.* **20**(6), 066010 (2015).
49. S. Tzoumas et al., "Effects of multispectral excitation on the sensitivity of molecular optoacoustic imaging," *J. Biophotonics* **8**(8), 629–637 (2015).

Biographies of the authors are not available.